Two-dimensional drift-diffusion study of mid-gap states and subsequent vacuum level shifts at interfaces in bulk-heterojunction solar cells

Christian Ahläng,[1] Oskar J. Sandberg,[2, 1] and Ronald Österbacka[1]

[1]*Physics, Department of Science and Engineering,*
Center for Functional Materials, Åbo Akademi University,
Porthaninkatu 3, 20500, Turku, Finland
[2]*Department of Physics, Swansea University,*
Singleton Park, Swansea SA2 8PP Wales, United Kingdom

Abstract

In recent years, there have been numerous observations of large vacuum level shifts, often attributed to the presence of mid-gap states, at many different metal/organic and organic/organic interfaces. Many of the same interfaces are found in bulk-heterojunction (BHJ) solar cells, where the large vacuum level shifts may alter the energy level alignment compared to common assumption. In this work, we have used a two-dimensional drift-diffusion simulation to calculate the vacuum level landscape for BHJ solar cells. We see that the large concentrations of mid-gap states required for experimentally observed vacuum level shifts to occur completely change the energetics of the device.

When such mid-gap states are present, at thermal equilibrium, we find that the vacuum level landscape is dominated by abrupt changes in the vacuum level at interfaces and a constant value for the vacuum level within the donor and acceptor phase. Under illumination, for mid-gap state depths larger than a certain threshold, the population of mid-gap states becomes dominated by the capture of free charge carriers. This behavior sets and upper limit for the electric field within the donor and acceptor phase, which is much smaller than typical values for the electric field in the device under operational conditions. Our results show that, in general, simply adding experimental values for vacuum level shifts obtained for the individual interface will not produce the real vacuum level landscape in the device. The magnitude of the vacuum level shift at any one interface not only depends on the surface density and energy of the mid-gap states at that interface, but also on the alignment at other interfaces throughout the device.

I. INTRODUCTION

The performance of organic solar cells is largely determined by processes occurring at interfaces, such as charge separation and recombination. Bulk-heterojunction (BHJ) solar cells takes this to the extreme by blending the electron-donating (donor) and electron-accepting (acceptor) material, forming an interconnected structure where interfaces between the two materials are effectively found everywhere throughout the active layer of the solar cell. In a BHJ solar cell, generated electron-hole pairs will diffuse to a nearby donor/acceptor interface where they are quickly dissociated into free electrons and holes of density n and p. Some of the energy of the absorbed photon is lost when the electron is transferred from the donor to the acceptor, and the maximum energy that can be extracted is limited by the difference between the highest occupied molecular orbital (HOMO) of the donor and the lowest unoccupied molecular orbital (LUMO) of the acceptor.[1,2] Another of the main loss mechanisms in BHJ solar cells is recombination, occurring when a free electron and hole meet at a donor/acceptor interface. In fact, the device performance of BHJ solar cells is mostly determined by processes occurring at interfaces in the device.[3,4]

After an electron-hole pair has been separated into free charge carriers, these are extracted by an internal electric field F. The magnitude of the electric field is determined by the work function of the anode Φ_{an} and cathode Φ_{cat}, the externally applied voltage and the shape of the vacuum level landscape inside the device. The electric field can be related to the vacuum level (VL) by way of the electric potential ψ. The electric field is given by $\bar{F} = -\nabla \psi$ and in this work, we have chosen the electric potential so that $-e\psi = \mathrm{VL}$, where e is the elementary charge. In the simplest case, at thermal equilibrium, the electric field is constant throughout the active layer, which corresponds to a linearly increasing or decreasing vacuum level. If there are abrupt changes in the potential at interfaces, seen as shifts in the vacuum level or band-bending depending on how far they extend from the interface, a much more complex situation may arise, such as that found in some organic light-emitting diodes.[5]

There have been many observations of large vacuum level shifts and band-bending at organic/metal and organic/organic interfaces, mainly in photoelectron spectroscopy studies in recent years.[6–13] Several different origins for vacuum level shifts and band-bending have been proposed, among others the induced density of interface states (IDIS)[14] and the integer charge transfer (ICT)[11] model, as well as a broad density of states for the HOMO and LUMO

3

levels[13,15]. Both the ICT and IDIS model are based on the existence of allowed states in the middle of the gap between the HOMO and the LUMO. These models describe how vacuum level shifts occur under such circumstances, when the normally unoccupied mid-gap states start to fill up. Similarly, when a large amount of charge carriers reside in the tail of a broad HOMO or LUMO density of states at an interface, band-bending or vacuum level shifts arise there.

The induced density of interface states model describes how the overlap between the wave function of the metal density of states and the molecular energy levels of the organic leads to an induced (continuous) density of interface states in the HOMO/LUMO gap of the organic. By calculating the IDIS and determining the charge neutrality level (CNL) and the slope parameter S, which depends on the screening properties of the material, the model is able to determine the size of the vacuum level shift at the surface in question.[14] The model has also been used to describe energy level alignment at organic/organic interfaces, based on the fact that the CNL is largely independent of the properties of the metal at the interface and can be considered a material-dependent property.[16]

The ICT model is based on integer charge transfer between a metal surface and an organic semiconductor when there is no hybridization between the metal DOS and the molecular orbitals of the semiconductor, for example due to the metal being passivated by hydrocarbons before deposition of the semiconductor. In the simplest approach, the model considers two (relaxed) levels located in the HOMO/LUMO gap, E_{ICT+} and E_{ICT-}, which have a positive and negative charge if occupied, respectively, and are taken to be properties of the semiconductor and therefore have the same energies at all interfaces.[11] At a metal/organic interface, charge may be transferred between the metal and the states E_{ICT+} and E_{ICT-} of the semiconductor, as well as between the ICT levels at organic/organic interfaces. Energy level alignment at metal/organic and organic/organic is predicted by considering if it is energetically favorable for charge carriers to be transferred across interfaces to these states.

In this work, we have clarified how mid-gap states located at metal/organic and organic/organic interfaces affect the vacuum level landscape in BHJ devices utilizing a two-dimensional drift-diffusion simulation. Drift-diffusion simulations have been used widely to model the device performance of and experimental results for organic solar cells. BHJ solar cells have often been modelled using one-dimensional drift-diffusion simulations, by utilizing effective parameters, to great success.[17–22] A two-dimensional simulation makes it possible

to directly include the morphology of the active layer and thereby effects occurring at interfaces. Two-(and three-)dimensional simulations have previously been used in several studies for relating the morphology of the active layer to the overall device performance.[23–27] In this work, we have expanded upon these results by including mid-gap states at interfaces in our two-dimensional drift-diffusion simulation.

II.   THEORETICAL BACKGROUND

In our model, we have assumed that the energy of the mid-gap states for a single material have the same energy at each of that materials interfaces. In the donor (acceptor), the mid-gap state has an energy E_+ (E_-) and concentration N_+ (N_-). The sign in the index specifies the charge of the state when filled and both state are taken to be neutral when empty. The energy at which transport takes place has been denoted E_v^D for holes in the donor, E_c^D for electrons in the donor and similarly E_v^A and E_c^A for holes and electrons in the acceptor, respectively. The depth of the mid-gap states has been defines as $\Delta E_+ = E_+ - E_v^D$ and $\Delta E_- = E_c^A - E_-$. The energy levels of the donor and acceptor are shown in FIG. 1 (a). A negatively charged state close to the donor LUMO and a positively charged state close to the acceptor HOMO were determined to have no influence on the energy level alignment in any of the scenarios we wish to study and were therefore left out from our model.

Under ideal conditions, when the concentration of occupied mid-gap states is negligible, vacuum level alignment occurs, giving rise to an approximately constant electric field in the active layer of the device, as shown in FIG 1 (b). Vacuum level shifts on the order of tenths of an eV over only a few nanometers, as is typically reported, only arise for large concentrations of mid-gap states, similar to that of the HOMO and LUMO levels.[10,11,28] Above a certain threshold value for the concentration of mid-gap states, the Fermi-level becomes pinned to the energy of the mid-gap states at the electrode/organic interfaces.

For rather shallow mid-gap state depths, vacuum level shifts $\Delta_{\mathrm{an,D}}$ and $\Delta_{\mathrm{cat,A}}$ will only occur at the electrode interfaces while the rest of the potential difference between the electrodes drops over the active layer. For deep mid-gap states, when E_+ is higher in energy than E_-, a vacuum level shift $\Delta_{\mathrm{D/A}}$ may also arise at the donor/acceptor interface. FIG. 1 (c) shows a situation where the mid-gap states throughout the active layer become pinned to the (constant) Fermi level E_F at thermal equilibrium. When the thermal equilibrium is
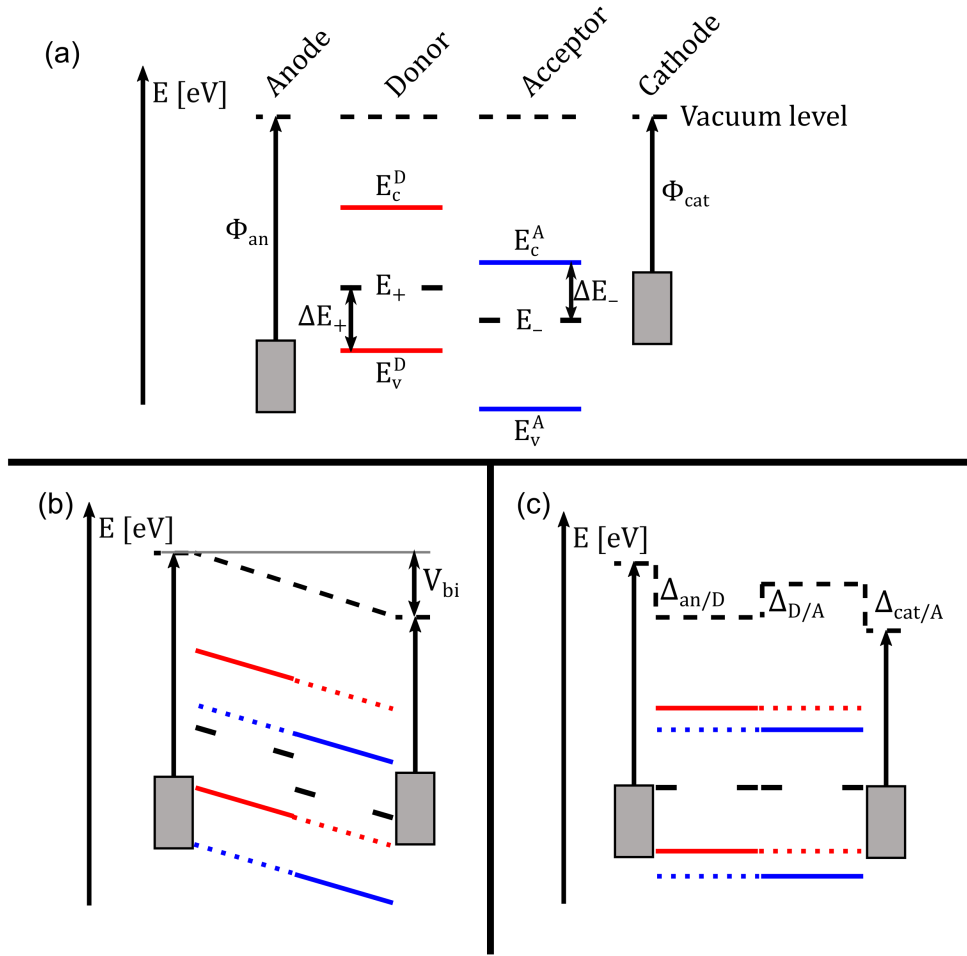
5

FIG. 1. Energy level diagram of the materials found in a typical BHJ solar cell, including mid-gap states. The mid-gap states E_+ and E_- are shown as shorter lines at interfaces. The vacuum level is shown by the dashed line at the top. (a) The energy levels of the isolated materials, relative to a common vacuum level. The dotted lines in FIG. (b) and (c) emphasize that donor and acceptor phases, and consequently, the transport levels are found throughout the active layer. (b) Vacuum level alignment after device fabrication, giving rise to a constant electric field in the device. (c) Pinning to mid-gap states after device fabrication, giving rise to large vacuum level shifts at interfaces. The vacuum level has a constant value within the material phases with large shifts at interfaces.

broken, as is the case under illumination or when an external potential is applied, it is not straightforward to determine the effects such states have on the device performance.

III. DRIFT-DIFFUSION SIMULATION

A. Model of Charge Transport in the Bulk

A two-dimensional drift-diffusion simulation solves a set of equations, which at steady state is made up of the continuity equation for holes

$$\frac{1}{e}\nabla \cdot \bar{J}_p(p, \psi) = G - R(p, n), \tag{1}$$

electrons

$$-\frac{1}{e}\nabla \cdot \bar{J}_n(n, \psi) = G - R(p, n) \tag{2}$$

and the Poisson equation

$$\nabla^2 \psi(x, y) = \frac{e}{\varepsilon\varepsilon_0}(n(x, y) + n_{E_-}(n, p, \psi) - p(x, y) - p_{E_+}(n, p, \psi)). \tag{3}$$

Here, x and y the two spatial dimensions, $\bar{J}_p$ and $\bar{J}_n$ the current densities for the respective charge carrier, G the generation rate, R the recombination rate, $\varepsilon\varepsilon_0$ the dielectric constant and n_{E_-} and p_{E_+} the concentrations of electrons and holes in mid-gap states. The dependence on the spatial dimensions for the charge carrier concentrations and electric potential is explicitly written out to emphasize that n, p and ψ are calculated as functions of these. All other variables can be expressed as functions of n, p and ψ, resulting in a system of three equations and three unknowns. The charge transport is modeled as the sum of drift and diffusion currents, leading to the following expressions for the current density of holes

$$\bar{J}_p(p, \psi) = -ep(x, y)\mu_p\nabla\psi(x, y) - kT\mu_p\nabla p(x, y) \tag{4}$$

and electrons

$$\bar{J}_n(n, \psi) = -en(x, y)\mu_n\nabla\psi(x, y) + kT\mu_n\nabla n(x, y). \tag{5}$$

The transport energy levels have been included so that holes are transported at energy E_v and electrons at E_c, each with an effective density of states N_v and N_c. The concentration

of free electrons and holes, provided that the Boltzmann approximation holds, are given by

$$p(x,y) = N_v \exp\left(\frac{E_v - E_F^p}{kT}\right)$$
$$n(x,y) = N_c \exp\left(\frac{E_F^n - E_c}{kT}\right), \tag{6}$$

where E_F^p and E_F^n are the quasi-Fermi levels of holes and electrons. The transport levels are shifted into the gap by $\sigma^2/2kT$ compared to the center of the HOMO and LUMO level DOS, where σ is the width of the Gaussian density of states of these.[29]

These equations describe the charge transport in the bulk of the materials and some remain valid even at interfaces, while others need to be examined further.

B.   Interface model

The benefit of using a two-dimensional model is that the morphology of the active layer of the solar cell can be included directly, which is especially important when studying interfacial effects. We define an interface in the model as two neighboring lattice points situated in two different materials.

The boundary condition at the electrodes include Schottky barriers, given by the difference between the electrode Fermi-level and the energy of a free charge carrier at their respective transport level, using Boltzmann statistics. At the anode, the concentrations are given by

$$p_{\mathrm{an/org}} = N_v \exp(-(E_F^{\mathrm{an}} - E_v^{\mathrm{org}} + e\psi_{\mathrm{org}})/kT)$$
$$n_{\mathrm{an/org}} = N_c \exp(-(E_c^{\mathrm{org}} - e\psi_{\mathrm{org}} - E_F^{\mathrm{an}})/kT) \tag{7}$$

where E_v^{org} and E_c^{org} are either the donor or acceptor value of E_v and E_c, ψ_{org} is the electric potential in the organic, next to the anode and $E_F^{\mathrm{an}} = -\Phi_{\mathrm{an}} - e\psi_{\mathrm{an}}$ is the Fermi-level of the anode. This way, the effects of large dipoles at this interface, effectively raising or lowering the barriers for injection, are included in $n_{\mathrm{an/org}}$ and $p_{\mathrm{an/org}}$.[28] The concentrations at the cathode are calculated in a corresponding manner.

Generation of free charge carriers was included in the model as a constant generation rate G at the donor/acceptor interface. Bimolecular recombination mainly occurs between a hole located in the donor p_D and an electron in the acceptor n_A. At the donor/acceptor

interface, the recombination rate was taken to be given by a Langevin-type expression,

$$R_{\text{bm}} = \gamma \beta_L (n_A\, p_D - n_i^2),\tag{8}$$

where the indices D and A refer to the parameter value in the donor and acceptor, respectively. Here, β_L is the Langevin recombination coefficient

$$\beta_L = \frac{q}{\varepsilon \varepsilon_0}(\mu_n^A + \mu_p^D),\tag{9}$$

γ is a reduction factor, n_A the electron concentration in the acceptor phase next to the interface, p_D the hole concentration in the donor phase next to the interface and n_i^2 the intrinsic charge carrier density, which ensures that the net recombination rate is zero at thermal equilibrium, given by

$$n_i^2 = N_v^D\, N_c^A \exp\left(\frac{E_v^D - e\psi_D - E_c^A + e\psi_A}{kT}\right).\tag{10}$$

The reduction factor γ is included to compensate for the low recombination rates typically observed in BHJ systems.[30]

The mid-gap states were included as single-level trap states in the model. In the donor (acceptor), mid-gap states with the energy E_+ (E_-) were assumed to be located at interfaces to both electrodes and the acceptor (donor) phase. The population of the mid-gap states were calculated utilizing SRH statistics.[31] The population of the E_+ state p_{E_+} at the donor/acceptor interface is given by

$$p_{E_+} = N_+ \frac{C_p\, p_D + C_n\, n_1}{C_n\,(n_A + n_1) + C_p\,(p_D + p_1)},\tag{11}$$

where $C_n = \frac{q}{\varepsilon \varepsilon_0}\mu_n^A$ and C_p are the capture coefficients for electrons and holes, which were taken to be equal for simplicity, and the terms p_1 and n_1 are given by

$$p_1 = N_v^D \frac{1}{\exp(\Delta E_+/kT) + 1}.\tag{12}$$

and

$$n_1 = N_c^A \frac{1}{\exp((E_+ - e\psi_D - E_c^A + e\psi_A)/kT) + 1}\tag{13}$$

The population of the E_- state was calculated in a corresponding manner.

Recombination via mid-gap states has been left out of this study for simplicity, since including it would require guessing another set of parameters, further increasing the complexity.

C. Simulation Parameters

The realistic and simplified morphologies used in this work are shown in FIG. 2. Periodic boundary conditions were used in the y-direction for both morphologies, so that $y = 0$ nm connects to $y = 20$ nm for structure (a) and $y = 10$ nm for structure (b). Structure (a) was drawn in order to demonstrate that the model works for a morphology resembling that found in a real device.[32] This structure does not contain any geometric symmetries, except for the periodic boundary conditions, which might affect the shape of the vacuum level landscape. The real, 3-dimensional structure also contains pathways in the third spatial dimension, which cannot be included directly in our 2-dimensional model. Therefore, this model should simply be seen as a way to study charge transport within continuous, elongated material structures.
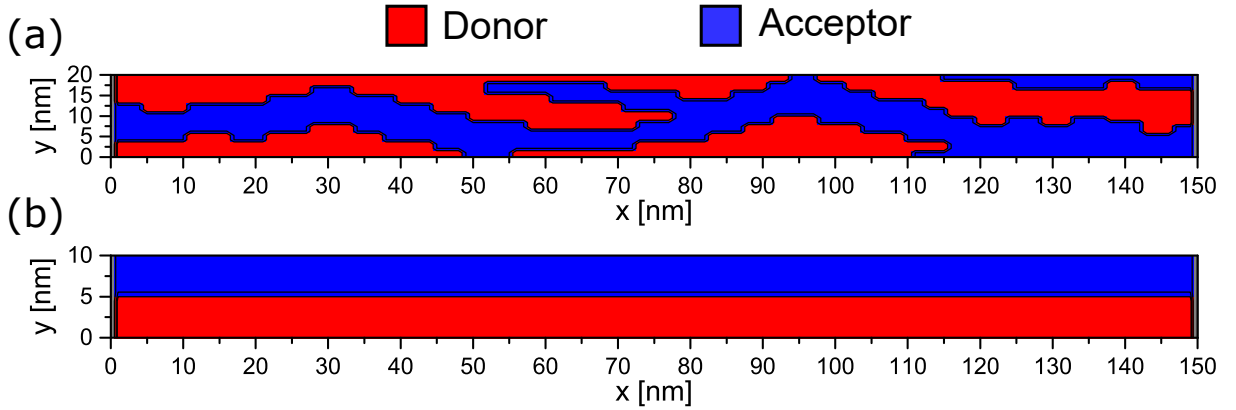

FIG. 2. (a) The realistic and (b) simplified morphology used for the calculations, referred to as structure (a) and (b). The donor is shown in red and the acceptor in blue and the anode is located at $x = 0$ nm and the cathode at $x = L = 150$ nm. Periodic boundary conditions have been applied for the y-axis, connecting $y = 0$ nm to $y = 20$ nm.

For all the simulations, we used the same concentrations of mid gap-states N_0 for both the donor and acceptor, so that $N_0 = N_+ = N_-$. In order to study the behavior for devices where the average thickness of the donor and acceptor phases does not vary along the x-direction, we chose the simplest possible case, structure (b) in FIG. 2.

The numerical implementation of the equations presented in this chapter are based on the procedure described by Selberherr[33]. The C++ code used to run the simulation can be downloaded at https://github.com/cahlang/2DDriftDif. The simulation parameters used in

TABLE I. Simulation parameters.

| Parameter	Donor value	Acceptor value	Parameter	Value
E_v [eV]	-4.8	-6.1	Φ_{an} [eV]	4.7
E_c [eV]	-2.8	-3.7	Φ_{cat} [eV]	3.8
μ_p, μ_n [cm^2/Vs]	10^{-3}	10^{-3}	G [1/cm^3]	1.5×10^{22}
N_c, N_v [1/cm^3]	10^{20}	10^{20}	γ	0.1
E_+, E_- [eV]	$-4.0 - -4.6$	$-3.9 - -4.5$	N_0 [1/cm^3]	$5 \times 10^{18} ... 10^{20}$
ε_r	3.4	3.4	T [K]	300

this work are shown in TABLE 1.

IV. RESULTS

In FIG. 3 (b) we show how pinning to mid-gap states occurs, both at the metal/organic and organic/organic interfaces with energies $\Delta E_+ = 0.8$ eV and $\Delta E_- = 0.6$ eV and concentrations $N_0 = 10^{20}$ cm^{-3} for structure (a). FIG. 3 (a) shows the vacuum level landscape without mid-gap states for comparison. The main features of the potential landscape are shifts in the vacuum level at interfaces and a constant vacuum level within the material phases. At the anode, vacuum level shifts of roughly $\Delta_{\mathrm{an/D}} = 0.7$ eV and $\Delta_{\mathrm{an/A}} = 0.4$ eV are seen at the donor and acceptor interfaces. Similarly, at the cathode interface, shifts of $\Delta_{\mathrm{cat/A}} = 0.5$ eV and $\Delta_{\mathrm{cat/D}} = 0.2$ eV are found for the acceptor and donor, respectively. At donor/acceptor interfaces throughout the active layer, a vacuum level shift of $\Delta_{\mathrm{D/A}} = 0.3$ eV is observed.

Note that the transport levels E_v^{D} and E_c^{A}, which are used as reference for the mid-gap state depths ΔE_+ and ΔE_-, are located 0.1 eV above and below the anode and cathode in energy, respectively. Therefore, if the Fermi level becomes pinned exactly to E_+ and E_-, vacuum level shifts that are 0.1 eV smaller than ΔE_+ and ΔE_- are to be expected. At the donor/acceptor interface, a vacuum level shift is expected to appear when E_+ is located higher in energy than E_-, that is when $\Delta E_+ + \Delta E_- \geq E_v^{\mathrm{D}} - E_c^{\mathrm{A}}$. If the Fermi level aligns exactly to E_+ and E_-, the shift at the donor/acceptor interface is given by $\Delta_{\mathrm{D/A}} = \Delta E_+ + \Delta E_- - 1.1$ eV, meaning that $\Delta_{\mathrm{D/A}} \leq 0.5$ eV with the simulation parameters
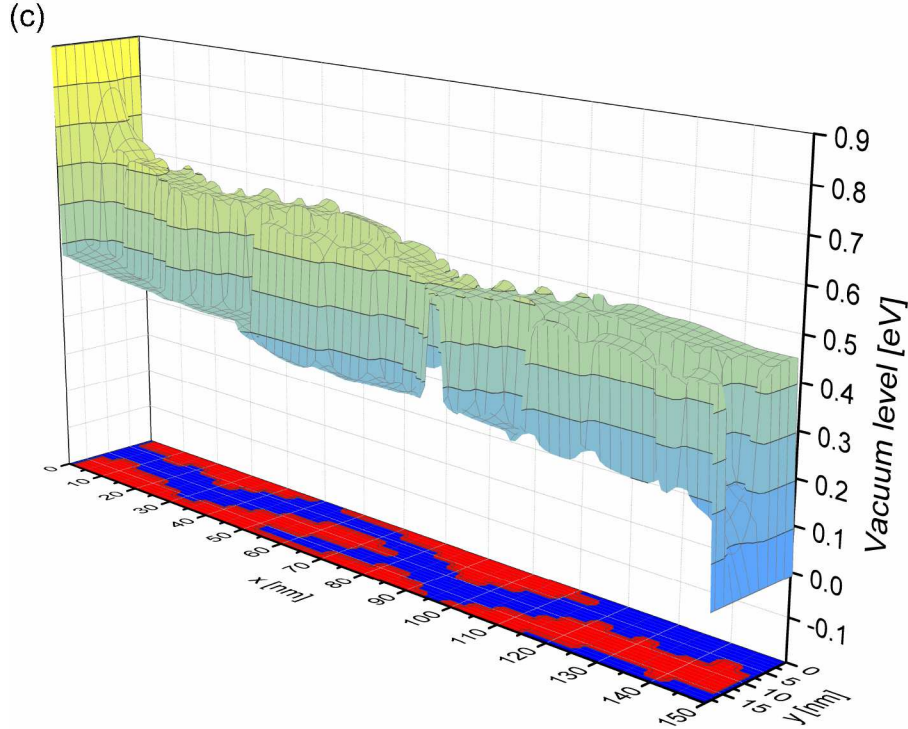
(a)

(b)

12
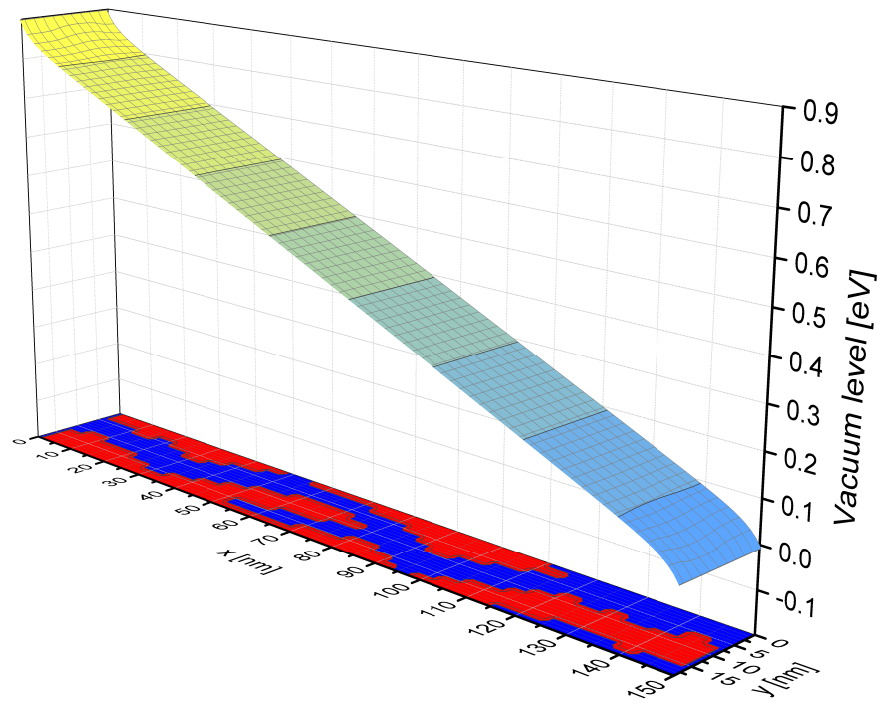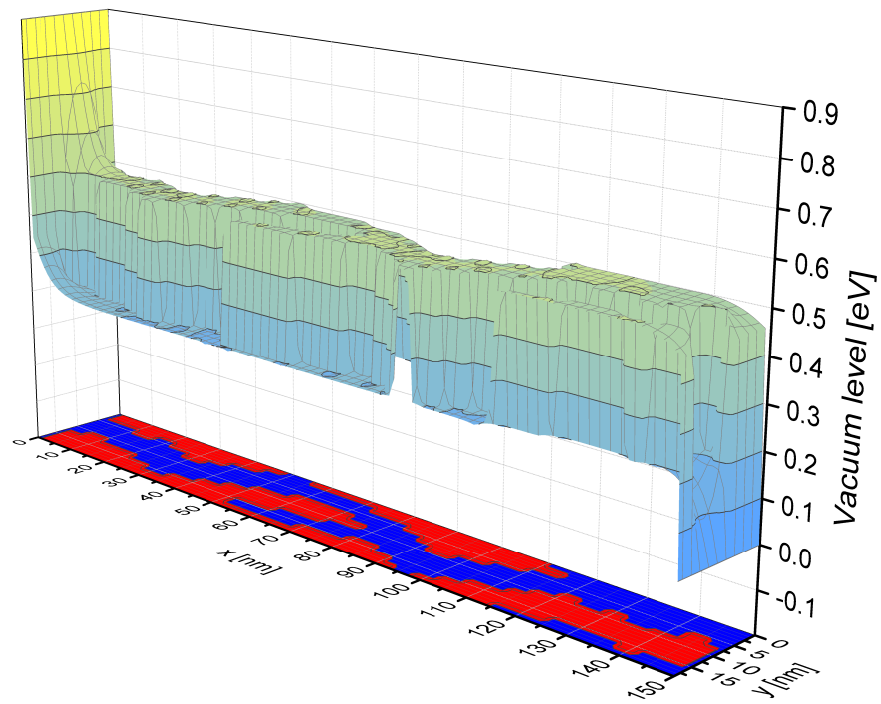
FIG. 3. The potential landscape in the active layer (a) without (b) with mid-gap states at thermal equilibrium and (c) with mid-gap states under illumination at short circuit. The projection at the bottom of the graphs shows the morphology of the active layer. The anode is located at $x = 0$ nm and the cathode at $x = 150$ nm and $y = 0$ nm is connected to $y = 19$ nm by the periodic boundary conditions.

used. The values seen in FIG. 3 (b) are almost exactly equal to these, meaning that the Fermi-level has aligned to E_+ and E_- throughout the active layer. This is also exactly the situation shown in FIG. 1 (c).

The most interesting result of the pinning situation in FIG. 3 (b) from a solar cell point of view is that there is no electric field within the donor and acceptor phases at thermal equilibrium. This is a direct result of the fact that mid-gap states, to which the Fermi-level is pinned, are found throughout the active layer at donor/acceptor interfaces in a BHJ solar cell.

Under illumination, at short circuit, the vacuum level is no longer constant in the bulk of the materials as seen in FIG. 3 (c). Here, the large free charge carrier concentrations,

$n, p \gg n_1, p_1$ in Eq. 11, in the device determine the population of mid-gap states throughout most of the device. Close to the electrodes, within a few nanometer thick region, the concentration of free charge carriers remains small and here vacuum level shifts similar to those at thermal equilibrium are retained. The result is a situation where mid-gap states at the electrodes build up large enough populations that the potential difference between the electrodes drops almost completely over these regions. In the rest of the device, the populations of the E_- and E_+ states are equal, resulting in an effectively charge-neutral region, over which the remaining potential difference, roughly 0.15 eV, drops linearly. Even though the vacuum level shifts here do not change noticeably, the mechanism for filling the mid-gap states is completely different compared to that at thermal equilibrium.

Before delving deeper into the details of this behavior, we determined at what density of, and energy for, the mid-gap states Fermi-level pinning occurs at thermal equilibrium. Having seen that the vacuum level landscape is what one would expect for this highly asymmetrical morphology, we switch to structure b, in order to simplify the analysis. For these calculations, the vacuum level showed no or a very weak y-dependence (parallel to the electrodes) within the separate material phases and therefore the vacuum level for all the following calculations is only plotted as a function of x. The vacuum level in the donor phase is plotted from $x = 0$ to $x = L/2$ and the vacuum level in the acceptor phase from $x = L/2$ to $x = L$. The vacuum level shift at the donor/acceptor interface generally showed no x-dependence, and the (constant) value of $\Delta_{\mathrm{D/A}}$ can be read from the figures at $x = L/2$. It is important to remember that structure (b) in FIG. 2 was used in each case and donor/acceptor interfaces are therefore found throughout the active layer. A simple bilayer structure where the donor and acceptor are two distinct layers deposited on top of one another would not necessarily reproduce the vacuum level landscapes shown in this work.

The x-dependence of the vacuum level landscapes for different values of N_0 is illustrated in FIG. 4. The calculations were done ranging from the value for N_0 used above, 10^{20} cm^{-3}, to 5×10^{18} cm^{-3}. In each case, the vacuum level shift at the donor/acceptor interface had a constant value throughout the active layer. Sharp vacuum level shifts, where the potential drop occurs over a few nanometers, are observed for $N_0 \geq 2.5 \times 10^{19}$ cm^{-3}, while the region over which the potential drops extends much further into the active layer for smaller values of N_0. As the concentration of mid-gap states is lowered from $N_0 = 2.5 \times 10^{19}$ cm^{-3}, a
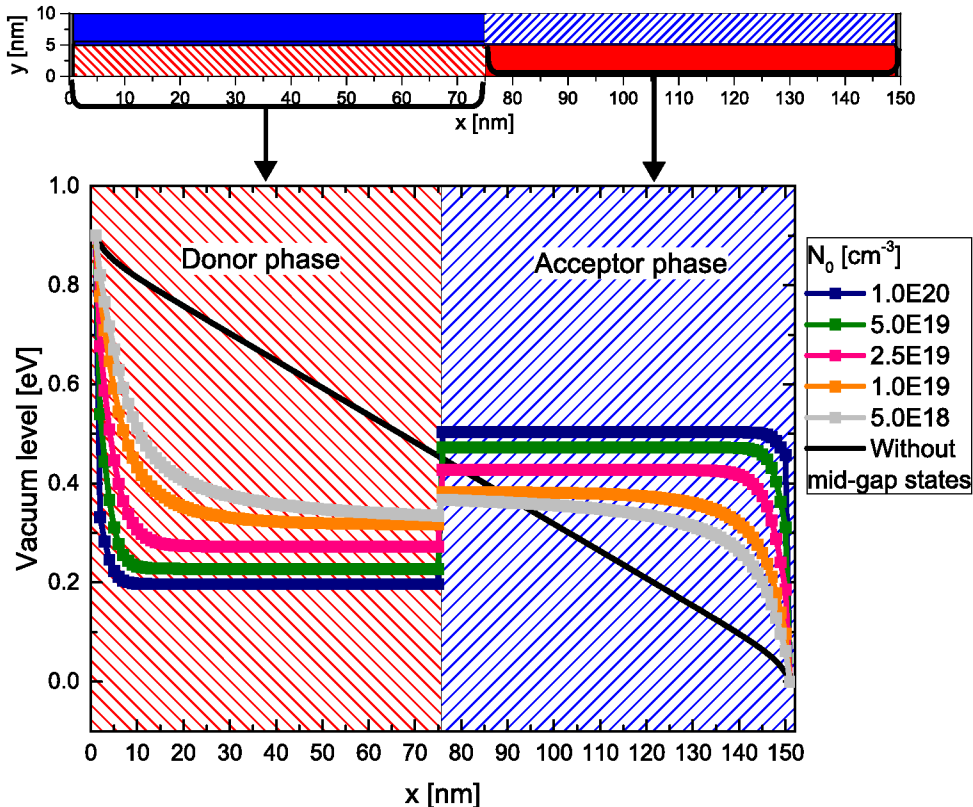
FIG. 4. The vacuum level at thermal equilibrium as a function of x, for different values of N_0 with $\Delta E_+ = 0.8$ eV and $\Delta E_- = 0.6$ eV. The region $0 < x < L/2$ shows the vacuum level in the donor phase and $L/2 < x < L$ the vacuum level in the acceptor phase.

large enough charge concentration for sharp vacuum level shifts to occur can no longer be reached, even if essentially all the states are filled. The charge concentrations are, however, still large enough to significantly alter the potential landscape in the active layer. For $N_0 \geq 2.5 \times 10^{19}$ cm^{-3}, the vacuum level reaches a constant value within 15 nm from the electrodes but is seen to saturate to different values for the different concentrations. The length scale of experimentally observed vacuum level shifts varies from system to system, but here we chose to focus on sharp vacuum level shifts for which the potential drops over a few nanometers. Therefore, all the remaining simulations were done with $N_0 = 10^{20}$ cm^{-3}.

Next we compare how the depth of the mid-gap states affect the vacuum level landscape, starting with equal depths for both mid-gap states, $\Delta E_+ = \Delta E_- = \Delta E_0$. The x-dependence of the vacuum level within the material phases is illustrated in FIG. 5. For $\Delta E_0 = 0.2$ eV, there is a shift in the vacuum level of roughly 0.1 eV at each of the electrodes while the
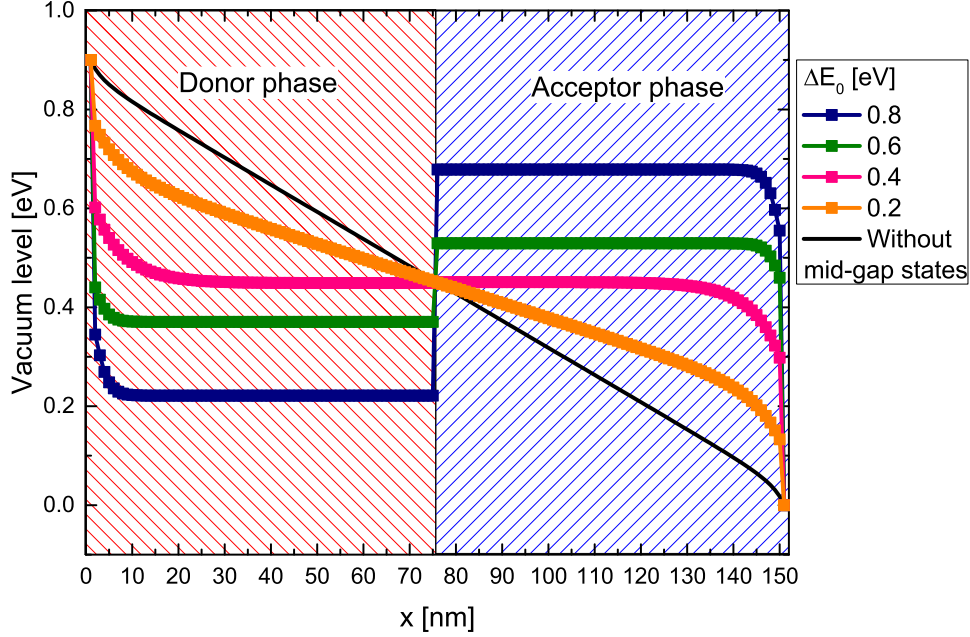
15

FIG. 5. The vacuum level at thermal equilibrium as a function of x, for different values of ΔE_0 with $N_0 = 10^{20}$ cm^{-3}. The region $0 < x < L/2$ shows the vacuum level in the donor phase and $L/2 < x < L$ the vacuum level in the acceptor phase.

rest of the potential difference between the electrodes drops more or less linearly over the active layer. For $\Delta E_0 = 0.4$eV, sharp vacuum level shifts $\Delta_{\mathrm{an/D}} = \Delta_{\mathrm{cat/A}} = 0.3$ eV are followed by an additional drop of 0.15 eV over 15 nm at the electrodes. The initial shifts of 0.3 eV already align the Fermi level to E_+ and E_-, but a significant amount of charge in mid-gap states along the donor/acceptor interfaces causes the vacuum level to drop further. Consequently, at a distance of 15 nm from the electrodes, the Fermi level is aligned 0.15 eV above E_+ and 0.15 eV below E_-. The vacuum level is constant throughout the rest of the active layer. As ΔE_0 increases, the region over which the potential drops at the electrodes becomes narrower and the vacuum level reaches a constant value about 5 nm into the active layer. In each case, we see that $\Delta_{\mathrm{an/D}}$ and $\Delta_{\mathrm{cat/A}}$ deviates only slightly from the expected value $\Delta E_0 - 0.1$ eV.

Under illumination, at zero applied voltage, the shape of the vacuum level landscape, shown in FIG. 6, is very similar for all cases with $\Delta E_0 \geq 0.4$ eV. For these values of ΔE_0, we see that $\Delta_{\mathrm{an,D}} \approx \Delta_{\mathrm{cat,A}} \approx 0.5$ eV, falling over a more narrow region with increasing values of ΔE_0 and a small electric field appears in the previously field-free region. For
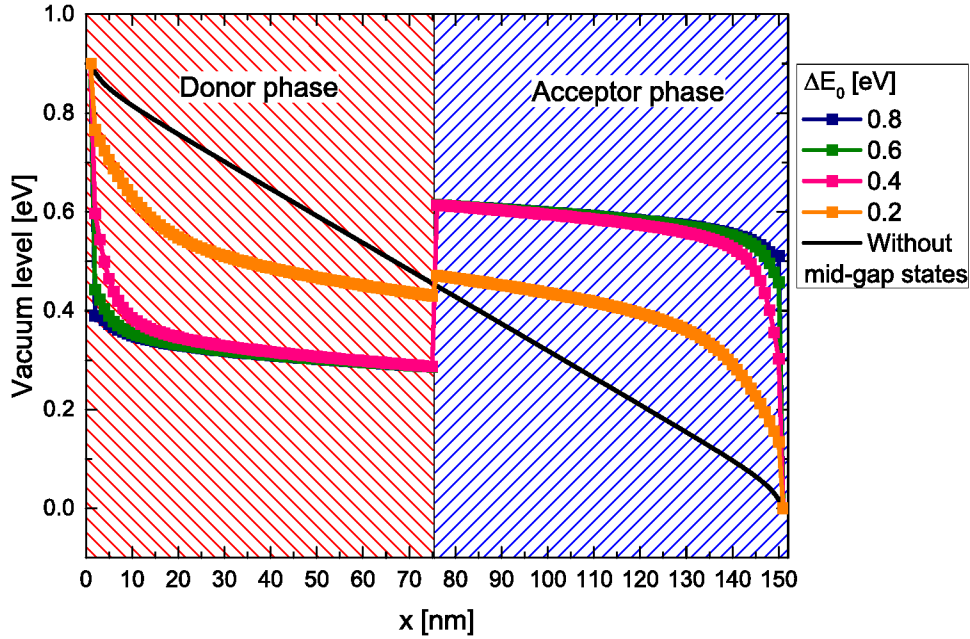
16

FIG. 6. The vacuum level under illumination, at short circuit as a function of x, for different values of ΔE_0. The region $0 < x < L/2$ shows the vacuum level in the donor phase and $L/2 < x < L$ the vacuum level in the acceptor phase.

$\Delta E_0 = 0.2$ eV, the vacuum level landscape deviates significantly from that seen for larger values of ΔE_0, since p_1 and n_1 in Eq. (11) are of similar magnitude as the concentrations of free charge carriers in this case. At short circuit, the electric field in the active layer, within the donor and acceptor phases, corresponds to a potential drop of roughly 0.1 eV over the whole device.

When a negative voltage is applied, the electric field within the donor and acceptor phases increases slightly, but remains very small compared to the case without mid-gap states. FIG. 7 (a) shows the electric field at the center of the device, $F_{L/2}$, within the donor phase, plotted as a function of applied voltage for the different mid-gap state depths. FIG. 7 (b) shows the current through the device under illumination, demonstrating the effect of a limited internal field on the performance of the device. The small internal electric field results in poor extraction of generated charge carriers and consequently a noticeable recombination, seen as a decrease in the photocurrent with increasing ΔE_0. The appearance of a S-shape in the IV curve and a large reduction in the open circuit voltage with increasing ΔE_0 is also observed.
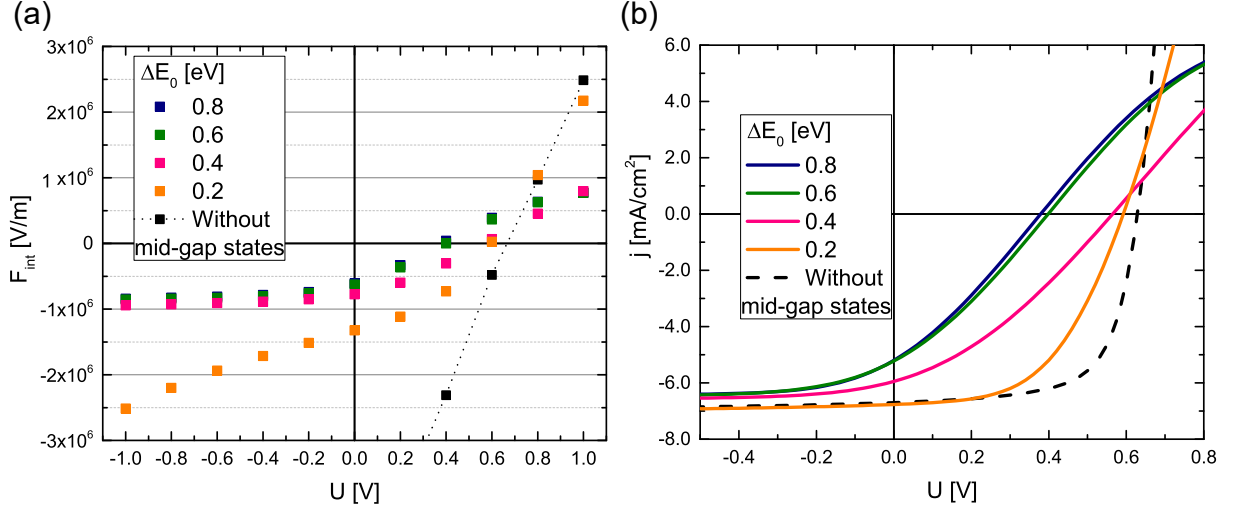
17

FIG. 7. (a) The internal electric field at $x = L/2$, $y = 2.5$ nm as a function of external voltage for different mid-gap state depths ΔE_0. (b) The current as a function of external voltage for different mid-gap state depths

So far we have only looked at situations where ΔE_+ and ΔE_- are similar or equal. In the following simulations, we chose a constant value for E_+ and studied how the vacuum level landscape changes with changing E_-. The vacuum level landscapes for $\Delta E_+ = 0.2$ eV and $\Delta E_+ = 0.8$ eV at thermal equilibrium and under illumination at short circuit are shown as a function of x in FIG. 8.

For $\Delta E_+ = 0.2$ eV, shown in FIG. 8 (a), the Fermi level aligns roughly to E_- at a few nanometers into the active layer, seen as shifts of roughly $\Delta_{\text{cat/A}} = \Delta E_- - 0.1$ eV. For $\Delta E_- = 0.4$ eV and $\Delta E_- = 0.6$ eV, the vacuum level changes by an additional 0.1 eV within a 15 nm thick region. At the anode, the initial shift in the vacuum level $\Delta_{\text{an/D}} \approx 0.15$ eV over a few nanometers is the same in all cases, but for $E_- = 0.4$ eV and $E_- = 0.6$ eV the vacuum level drops further in the same way as was seen at the cathode. For $\Delta E_- = 0.2$ eV, the remaining potential difference drops linearly over the active layer and for $\Delta E_- = 0.8$ eV a small vacuum level shift $\Delta_{\text{D/A}} = 0.05$ eV appears at the donor/acceptor interface. Under illumination, the vacuum level landscape is almost identical for all values of ΔE_-. In the donor phase, the vacuum level is very similar to that at thermal equilibrium with $\Delta E_- = 0.8$ eV. At the cathode/acceptor and the donor/acceptor interface, shifts of $\Delta_{\text{cat/A}} \approx 0.7$ eV and $\Delta_{\text{D/A}} \approx 0.12$ eV are seen for all values of ΔE_-.

For $\Delta E_+ = 0.8$ eV, the Fermi level aligns close to E_- at the cathode for all values of
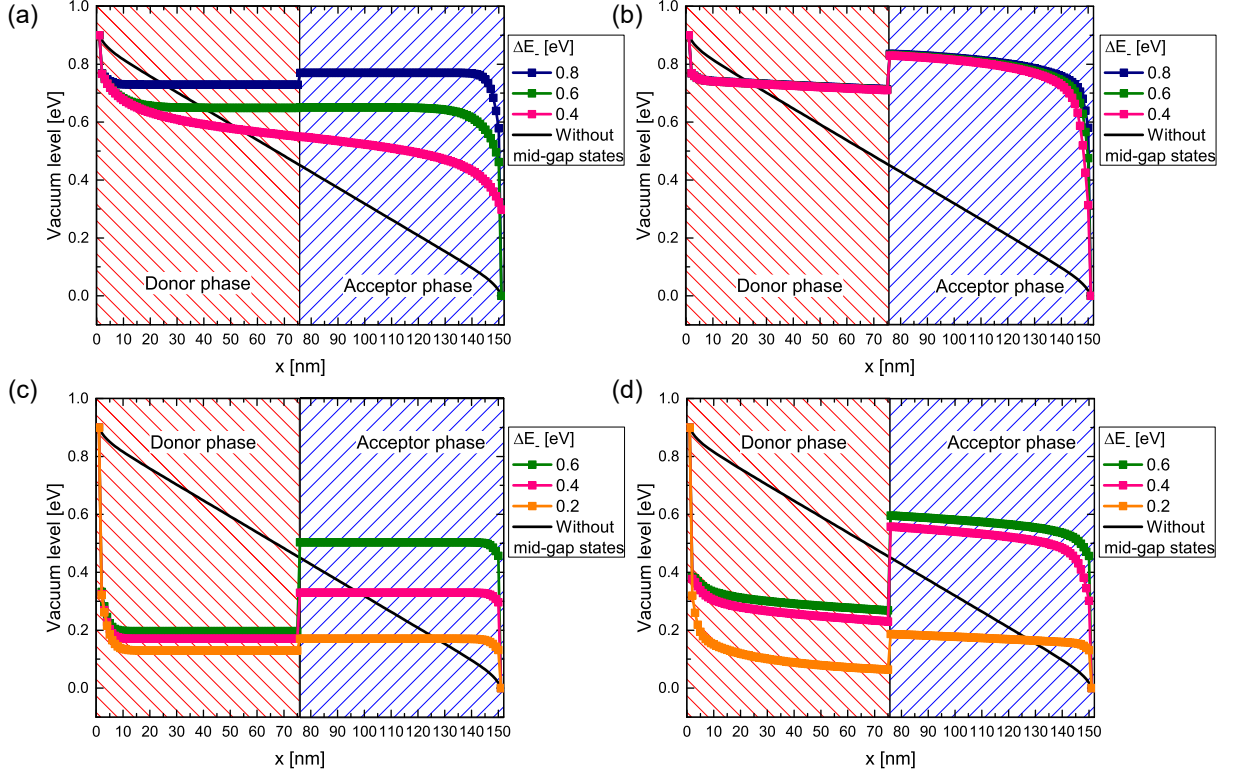
18

FIG. 8. The vacuum level as a function of x for different values of ΔE_-. The region $0 < x < L/2$ shows the vacuum level in the donor phase and $L/2 < x < L$ the vacuum level in the acceptor phase. a) $\Delta E_+ = 0.2$ at thermal equilibrium. b) $\Delta E_+ = 0.2$ eV under illumination at short circuit. c) $\Delta E_+ = 0.8$ at thermal equilibrium. d) $\Delta E_+ = 0.8$ eV under illumination at short circuit.

ΔE_-. At the anode, the vacuum level shift changes noticeably for the different values of ΔE_- but the Fermi-level remains aligned close to E_+ and $\Delta_{\mathrm{an/D}} \approx 0.7$ eV in all cases. The vacuum level is constant throughout most of the active layer and $\Delta_{\mathrm{A/D}}$ has a non-zero value in all cases. Under illumination, for $\Delta E_- = 0.2$ eV, the vacuum level shifts at the electrodes change only slightly from those observed at thermal equilibrium, while the vacuum level shift at the donor/acceptor interface increases slightly. For $\Delta E_- = 0.4$ eV and $\Delta E_- = 0.6$ eV, the shape of the vacuum level is very similar in both cases, except shifted by about 0.05 eV with respect to an another. The shape of this vacuum level landscape is also identical, expect for a small shift downwards in energy, to that for $\Delta E_0 \geq 0.4$ eV in FIG. 6.

V. DISCUSSION

Values for many of the parameters relating to vacuum level shifts at interfaces have still not been determined experimentally and therefore we have used as simple a model as possible for the mid-gap state in this work. Although our model is simplified, we expect that the results presented in this work are of qualitative relevance. In reality, the DOS of the mid-gap states has some width and shape, but we expect that the effect of, for example, a Gaussian DOS will look like an effectively smaller or larger depth for the mid-gap states when the DOS is either almost full or almost empty, based on a similar result for the transport levels in a study by J. C. Blakesley and N. C. Greenham[29]. In most of the situations presented in this study, the population of the mid-gap states is close to half the concentration of states and therefore any DOS which is symmetric around E_+ and E_- should deviate very little from the results presented in this work. Especially under illumination, we expect that the exact depth and shape of the DOS of the mid-gap states is of minor importance for mid-gap state depths above a certain threshold value, based on the results presented in FIG. 6.

In order to gain a better understanding of the charge transport under illumination we investigated this from an analytical point of view. For mid-gap states depths larger than a certain threshold, $\Delta E_+ \geq 0.4 \text{eV}$ and $\Delta E_- \geq 0.4$ eV with the parameters used in this work, we have shown that the electric field throughout most of the device remains very small even when a voltage is applied. In this region of the active layer, $\delta < x < L - \delta$, the shape of the charge carrier concentrations are determined by diffusion and can be calculated analytically if the drift component of the current is neglected and the recombination is negligible.[34] Assuming that the concentrations of free charge carrier concentration at $x = \delta$ and $x = L - \delta$ are small compared to those in the bulk, these are given by

$$
\begin{aligned}
p(x) &= \frac{eG_{\text{eff}}}{2\mu_p kT}(x - \delta)(L - x - \delta) \\
n(x) &= \frac{eG_{\text{eff}}}{2\mu_n kT}(x - \delta)(L - x - \delta)
\end{aligned}
\tag{14}
$$

where G_{eff} is an effective generation rate. The calculated charge carrier concentrations were also confirmed to have this shape.

In this case, when $n, p \gg n_1, p_1$, the population of the mid-gap states are dominated by free charge carriers and p_1 and n_1 can be neglected in Eq. (11). The population of the

mid-gap states then becomes

$$p_{E_+} = N_+ \frac{C_p p}{C_n n + C_p p}$$
$$n_{E_-} = N_- \frac{C_n n}{C_n n + C_p p}. \tag{15}$$

With the expressions we used for the capture coefficients and when the charge carrier concentrations are given by Eq. (14), the population of the mid-gap states becomes $p_{E_+} = n_{E_-} = N_0/2$ and in the region $\delta \leq x \leq L - \delta$. In this region the potential landscape is therefore completely independent of the mid-gap state depths, as long as these are large enough. This is seen especially well when comparing FIG. 6 and 8 (d), where the vacuum level landscapes are almost identical in the region 10 nm $\leq x \leq 140$ nm but shifted relative to each other due to the different vacuum level shifts at the electrodes.

The x-dependence of any electric field in this region can be calculated by utilizing the divergence theorem, stating that $\nabla j(x) = 0$ in one dimension. The field must therefore have the form

$$F(x) = F_{L/2} \frac{(L/2 - \delta)^2}{(x - \delta)(L - x - \delta)}. \tag{16}$$

The net current through the device, using the expressions for the charge carrier concentrations and the electric field in Eq. (14) and (16), is then given by

$$j_{\text{net}} = j_{\text{drift}}^p + j_{\text{drift}}^n = -\frac{e^2 G_{\text{eff}}}{kT} F_{L/2} (L/2 - \delta)^2. \tag{17}$$

As shown by FIG 7 (a), $F_{L/2}$ is only weakly dependent on the applied voltage for deep mid-gap states and therefore also the current in reverse bias. When an external voltage is applied, most of the potential difference between the electrodes drops close to the electrodes within the region δ, while the electric field within the materials phases throughout most of the device remain mostly unaffected. The reduction in the open circuit voltage and the S-shaped IV-curves can be understood based on increasing effective injection barriers with increasing ΔE_0.[19]

The concentration of mid-gap states required for sharp vacuum level shifts to occur in our model was determined to be roughly 2.5×10^{19} cm^{-3}, while lower concentrations give rise to band bending extending tens of nanometers into the active layer. This concentration in our model corresponds to a surface density of 1.25×10^{12} cm^{-2} for the anode and cathode interfaces. In a BHJ solar cell, the effective surface density of interface states at the electrodes

is influenced by the donor:acceptor blend ratio. In devices with a high:low blend ratio, this might lead to a significantly different vacuum level landscape at the cathode compared to experimental values obtained for bilayer structures in photoelectron spectroscopy studies.

Compared to the IDIS and ICT model, our simulation with single-level mid-gap states is quite different compared to the IDIS model but resembles the ICT model more closely. Due to the comparatively large distance between the metal surface and the location of the mid-gap states used in this study, relative to that in the IDIS model, no direct comparison is possible at the metal/organic interfaces. However, we note that the typical surface density of mid-gap states in the IDIS model is of the order 5×10^{13} cm^{-2}, which is at least an order of magnitude larger than the values used in this work.[10] In the limit of a very large surface density of interface states, the Fermi-level aligns close to the CNL in energy and in this case E_+ and E_- should be taken to be located just below and above the CNL in energy, respectively.[28]

The simulations of the energy level alignment at thermal equilibrium show that the Fermi-level does not always align exactly to the energy of the mid-gap states even for our single-level model. Instead, the exact energy alignment depends on both the concentration and depth of the states and even the alignment at the other electrode. This means that adjusting the energy level diagram for a BHJ solar cell by including experimentally obtained vacuum level shifts does not necessarily produce the real energy level alignment in the device.

The results presented in this work indicate that the effect that mid-gap states, which give rise to large vacuum level shifts, have on the device performance of BHJ solar cells are much more complex than one might expect. This study highlights that when determining the energy level alignment in devices consisting of multiple layers and/or blends, one cannot simply measure the vacuum level shift at each interface separately. The two-dimensional drift-diffusion simulation used in this work has proven to be a useful tool for studying energy level alignment in complex devices, but in order to obtain quantitative values, a comprehensive model of mid-gap states is required.

VI. CONCLUSIONS

In this work we have determined how mid-gap states leading to large vacuum level shifts at interfaces affect the vacuum level landscape in BHJ solar cells. We have shown how the

energy level alignment in a device cannot be determined simply by adding experimentally obtained vacuum level shifts. The exact energy to which the Fermi-level aligns at one of the electrodes depends on both the surface density and energy of the mid-gap state, as well as the exact energy level alignment at the other electrode.

Under illumination, we show how the population of mid-gap states, which have a depth that is larger than a certain threshold, at the donor/acceptor interface become dominated by free charge carriers. When this occurs, most of the potential difference between the electrodes drops over a few nanometer thick region at the electrodes. The electric field in the active layer remains very small even when an external voltage is applied, preventing efficient charge extraction.

VII.   ACKNOWLEDGMENTS

[1] L. J. A. Koster, V. D. Mihailetchi, and P. W. M. Blom, Appl. Phys. Lett. **88**, 093511 (2006).

[2] G. Dennler, M. C. Scharber, and C. J. Brabec, Adv. Mater. **21**, 1323 (2009).

[3] P. W. M. Blom, V. D. Mihailetchi, L. J. A. Koster, and D. E. Markov, Adv. Mater. **19**, 1551 (2007).

[4] B. C. Thompson and J. M. J. Fréchet, Angew. Chem. Int. Ed. Engl. **47**, 58 (2008).

[5] S. Olthof, R. Meerheim, M. Schober, and K. Leo, Phys. Rev. B **79**, 245308 (2009).

[6] Q. Bao, O. Sandberg, D. Dagnelund, S. Sandén, S. Braun, H. Aarnio, X. Liu, W. M. Chen, R. Österbacka, and M. Fahlman, Adv. Funct. Mater. **24**, 6309 (2014).

[7] Z. Xu, L.-M. Chen, M.-H. Chen, G. Li, and Y. Yang, Appl. Phys. Lett. **95**, 013301 (2009).

[8] H. Aarnio, P. Sehati, S. Braun, M. Nyman, M. P. De Jong, M. Fahlman, and R. Österbacka, Adv. Energy Mater. **1**, 792 (2011).

9 A. Guerrero, L. F. Marchesi, P. P. Boix, S. Ruiz-Raga, T. Ripolles-Sanchis, G. Garcia-Belmonte, and J. Bisquert, ACS Nano **6**, 3453 (2012).

10 J. Hwang, A. Wan, and A. Kahn, Mater. Sci. Eng. R Rep. **64**, 1 (2009).

11 S. Braun, W. R. Salaneck, and M. Fahlman, Adv. Mater. **21**, 1450 (2009).

12 H. Ishii, K. Sugiyama, E. Ito, and K. Seki, Adv. Mater. **11**, 11 (1999).

13 I. Lange, J. C. Blakesley, J. Frisch, A. Vollmer, N. Koch, and D. Neher, Phys. Rev. Lett. **106**, 216402 (2011).

14 H. Vázquez, F. Flores, R. Oszwaldowski, J. Ortega, R. Pérez, and A. Kahn, Appl. Surf. Sci. **234**, 107 (2004).

15 M. Oehzelt, N. Koch, and G. Heimel, Nat. Commun. **5**, 4174 (2014).

16 H. Vázquez, W. Gao, F. Flores, and A. Kahn, Phys. Rev. B **71**, 041306(R) (2005).

17 T. Kirchartz, T. Agostinelli, M. Campoy-Quiles, W. Gong, and J. Nelson, J. Phys. Chem. Lett. **3**, 3470 (2012).

18 T. Kirchartz, W. Gong, S. a. Hawks, T. Agostinelli, R. C. I. MacKenzie, Y. Yang, and J. Nelson, J. Phys. Chem. C **116**, 7672 (2012).

19 O. J. Sandberg, M. Nyman, and R. Österbacka, Phys. Rev. Appl. **1**, 024003 (2014).

20 U. Würfel, D. Neher, A. Spies, and S. Albrecht, Nat. Commun. **6**, 1 (2015).

21 W. Tress, K. Leo, and M. Riede, Phys. Rev. B **85**, 155201 (2012).

22 T. Kirchartz, B. E. Pieters, J. Kirkpatrick, U. Rau, and J. Nelson, Phys. Rev. B **83**, 115209 (2011).

23 G. A. Buxton and N. Clarke, Phys. Rev. B **74**, 085207 (2006).

24 G. A. Buxton and N. Clarke, Model. Simul. Mater. Sci. Eng. **15**, 13 (2007).

25 F. F. Stelzl and U. Würfel, Phys. Rev. B **86**, 075315 (2012).

26 Y. Min Nam, J. Huh, and W. Ho Jo, Sol. Energy Mater. Sol. Cells **94**, 1118 (2010).

27 L. J. A. Koster, O. Stenzel, S. D. Oosterhout, M. M. Wienk, V. Schmidt, and R. A. J. Janssen, Adv. Energy Mater. **3**, 615 (2013).

28 S. M. Sze and K. K. Ng, *Physics of semiconductor devices*, 3rd ed. (John Wiley & Sons, 2006) pp. 134–196.

29 J. C. Blakesley and N. C. Greenham, Jour. Appl. Phys. **106**, 1 (2009).

30 A. Pivrikas, N. S. Sariciftci, G. Juška, and R. Österbacka, Prog. Photovolt. Res. Appl. **15**, 677 (2007).

[31] W. Shockley and W. T. Read, Phys. Rev. **87**, 835 (1952).

[32] J. S. Moon, J. K. Lee, S. Cho, J. Byun, and A. J. Heeger, Nano Lett. **9**, 230 (2009).

[33] S. Selberherr, *Analysis and Simulation of Semiconductor Devices* (Springer-Verlag, New York, NY, USA, 1984) pp. 127–144.

[34] R. Sokel and R. C. Hughes, J. Appl. Phys **53**, 7414 (1982).